W-band tunable, multi-channel, frequency comb Doppler backscattering diagnostic in the ASDEX-Upgrade tokamak

P. Molina Cabrera, W. Kasparek, T. Happel, H. Eixenberger, L. Kammerloher, P. Hennequin, K. Höfler, C. Honoré

W-band tunable, multi-channel, frequency comb Doppler backscattering diagnostic in the ASDEX-Upgrade tokamak

P. A. Molina Cabrera,[1, a)] W. Kasparek,[2] T. Happel,[1] H. Eixenberger,[1] L. Kammerloher,[1] P. Hennequin,[3] K. Höfler,[4] C. Honoré,[3] and the ASDEX Upgrade Team[b)]

[1)]*Max Planck Institute for Plasma Physics, Boltzmannstr. 2, 85748 Garching, Germany*

[2)]*IGVP, Universität Stuttgart, Pfaffenwaldring 31, 70569 Stuttgart, Germany*

[3)]*Laboratoire de Physique des Plasmas, Ecole Polytechnique, 91128 Palaiseau, France*

[4)]*Max Planck Institute for Plasma Physics, Wendelsteinstr. 1, 17491 Greifswald, Germany*

(*Electronic mail: pedro.molina@epfl.ch)

(Dated: 4 July 2023)

This article presents the design, implementation, and first data of a uniquely flexible, multi-channel, frequency comb Doppler backscattering diagnostic recently made operational in the ASDEX-Upgrade tokamak[1]. It uses a double sideband signal fed into a x6 frequency multiplier to produce a multiple-frequency output spectrum. Seven of these frequencies are simultaneously measured in the receiver via a two-step frequency down-conversion and traditional I/Q demodulation. The frequency comb spectrum is fully tunable to sit anywhere in the W-band. The inter-frequency separation is also uniquely tunable remotely between 0.1 and 6 GHz without any hardware changes. The diagnostic can be operated in both O and X-mode polarizations and at both oblique and normal incidence to the cutoff layer. The time evolution of backscattered signals, in excess of 30 dB, from 7 distinct frequencies sampled simultaneously are presented across an L to H-mode confinement regime transition.

I. INTRODUCTION

Moving towards an increased understanding of the dynamic processes in tokamak plasmas requires continuous innovation in diagnostic capabilities, pushing the envelope of both spatial and temporal resolutions. This article presents a uniquely flexible, multi-channel, heterodyne Doppler backscattering diagnostic (DBS) recently made operational in the ASDEX-Upgrade tokamak[1]. The DBS technique, first proposed over twenty years ago by Holzhauer et al.[2] consists of scattering a mm-wave at a frequency that encounters a cut-off in the plasma. Launched perpendicular to the main magnetic field and at an oblique angle with respect to the normal to the cut-off layer, the presence of intermediate wavenumber ($k_\perp = 3-15\,\mathrm{cm}^{-1}$) density fluctuations and an enhanced wave electric field in the vicinity of the cut-off leads to efficient and well-localized scattering of the incoming mm-wave beam according to the Bragg condition $k_\perp = -2k_i$ (where $\perp$ refers to fluctuations perpendicular to the main magnetic field, and i refers to incident at the scattering location). Using the same antenna as emitter and receiver measures the $m = -1$ scattering order. The power of the back-scattered signal is - in most cases - proportional to the amount of fluctuations at the selected k_i; although, there are documented circumstances where the back-scattered power can depend non-linearly on fluctuation level and scattering wavenumber[3–6]. Since the density fluctuations are rotating with respect to the laboratory frame, the back-scattered radiation is Doppler shifted by $\Delta\omega = \vec{v}\cdot\vec{k} \approx v_\perp k_\perp$ [7,8]. Using magnetic equilibrium and density profile information from other diagnostics, a ray or beam-tracing calculation[9] can be used to determine k_i and localize the scattering position, which then allows one to infer the velocity of fluctuations perpendicular to the main magnetic field ($v_\perp$). The latter is composed both of background and turbulence phase velocity components $v_\perp = v_{ExB} + v_{\mathrm{phase}}$. The DBS technique has demonstrated great potential to access key physics observables with minimal access requirements and no need to introduce impurities and/or particles in the plasma. The fast time resolution (sub-ms) and excellent spatial localization ($\sim$cm) of DBS has been exploited to infer high resolution $v_\perp$ plasma rotation profiles[10], intermediate wavenumber density fluctuation levels[8], wavenumber spectra[5], radial correlation lengths[11], time-dependent $E \times B$ shear flows[12], and, recently, the tilt angle of turbulent structures[13,14].

In most of these studies, a single, variable-frequency, heterodyne transceiver has been used. In such instruments, radial profiles are obtained by varying this single frequency in a staircase fashion, holding a constant frequency for a few ms (5−25 ms) and stepping it over the frequency band[15]. While this approach works well to study steady-state plasma conditions, many processes in the plasma edge such as the L-H transition[16] and edge-localized modes (ELMs)[17] occur in millisecond time scales and can significantly benefit from simultaneous multi-point probing[18]. Such measurements are possible if several simultaneous frequencies are launched into the plasma. Most approaches feature a constant inter-frequency separation termed a frequency *comb*.

Several technical approaches have been demonstrated to produce frequency combs, namely: frequency-modulated voltage-controlled-oscillators (VCO)[7], nonlinear-transmission lines (NLTL[19–22]), filter feedback loop microwave sources (FFLMS[23]), multiplexer-amplifier loops[24], and multi-frequency driven frequency multipliers[25–27]. More recently, Ren et al.[28] proposed multiple independent low-frequency synthesizers and multiplier pairs for each channel. Furthermore, Tokuzawa et al.[29] demonstrated how a comb spectrum on both transmitter and receiver

[a)]Current address: Ecole Polytechnique Fédérale de Lausanne (EPFL), Swiss Plasma Center (SPC), CH-1015 Lausanne, Switzerland

[b)]See author list of U. Stroth et al, 2022, Nucl. Fusion **62** 042006

stages can be used to bring multiple backscattered signals down to relatively low intermediate-frequencies ($<$0.5 GHz) which are then digitally sampled.

Most of these instruments output a particular frequency comb spectrum with fixed inter-frequency separation centered at a fixed position inside the microwave band and record the backscattered power of a fixed number of these frequencies using traditional I/Q demodulation[19–24]. A smaller subset of these instruments allow for the center frequency of the comb to be moved ('tuned') inside the band, but the receiver section uses fixed band-pass filters which allow to record backscattered power from a several frequencies exclusively at one particular inter-frequency separation[7,26,27]. Ren's[28] system is not formally a comb system since it features various output frequencies at arbitrary separation, and it is unable to change any of these frequencies without changing the receiver filter frequencies. There are only two implementations[25,29] that can change both the central frequency and inter-frequency separation of the comb output and measure the backscattered power from multiple frequencies without changes in hardware. However, both of these make use of large bandwidth digitizers:13 GHz[25] and 0.5 GHz[29] which can prove expensive and pose important data storage and subsequent analysis challenges.

This paper presents a new 7-channel DBS diagnostic using a double side-band frequency (three-tone) signal and a $\times 6$ frequency multiplier to produce a multi-frequency comb output in the W-band (75$-$110 GHz). The receiver features variable frequency synthesizers and an innovative double frequency down-conversion followed by traditional I/Q demodulation to measure the back-scattered signal from 7 frequencies simultaneously. The unique feature of this diagnostic is that both the central frequency of the comb output *and* the inter-frequency separation can be changed remotely without any hardware changes while traditional I/Q demodulation allows for regular digitizers (10 MHz bandwidth) to easily sample, store, and recall the 7-channel data. Thus, a single instrument can be used to monitor fast changes to global $v_\perp$ radial profiles using large inter-frequency separation as well as radial correlation lengths at small inter-frequency separations. Furthermore, the freedom to move the center of the frequency comb inside the W-band allows to sample a large range of plasma densities and magnetic fields. This instrument builds on a thorough proof-of-concept study presented by Happel et al.[30].

This paper begins by presenting the diagnostic design and implementation in section II. Power tuning and calibration is addressed in section III. First plasma data and conclusions then follow in sections IV and V.

II. HARDWARE DESIGN AND IMPLEMENTATION

Figure 1 shows a schematic diagram of the diagnostic setup. It consists of three main sections: a transmitter, receiver, and I/Q mixing stages. The transmitter produces a frequency-comb output in the W-band via a three-tone (double sideband) input to an active $\times 6$ frequency multiplier. This technique relies on the non-linear characteristics of the frequency multiplier and has been explained in detail by Happel et al.[30] in the case of a two-tone input. The same fundamental process occurs when using three-tone inputs. It has been empirically observed that using three-tone inputs leads to a better power flatness in the frequency-comb output. In order to create a three-tone input signal inside 12$-$18 GHz, mixer frequency up-conversion[31][p. 637] is used. This requires a balanced mixer and two separate signals, a local-oscillator (LO, f_0 in figure 1) and a relatively low-frequency modulation frequency (f_m). The result of the up-conversion is a double-sideband (DSB) signal $f_\mathrm{RF} = f_0 \pm f_\mathrm{m}$. The f_0 and f_m signals are created by two separate synthesizers: a high-frequency (12$-$18 GHz) National Instruments (NI) QuickSyn FSW0020 and a low-frequency ($<$6 GHz) Spectran SPS-06. The phase noise performance of these synthesizers, and those found in the receiver section discussed below, is shown in figure 2. This figure shows that the phase-noise performance is competitive (<-80 dBc/Hz for offset frequencies $f_o > 1$ KHz) with other synthesizers as well as FFLMs and non-linear transmission line circuit (NTLC) oscillators[23].

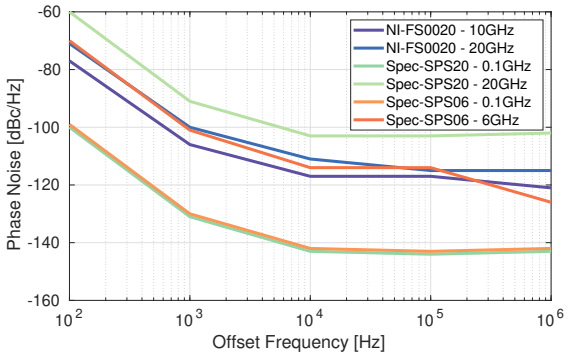

FIG. 2. Synthesizer single side band phase noise as a function of frequency offset from the carrier. The relevant output carrier frequency ranges for both NI (FSW0020 f $<$20 GHz) and Spectran (SPS-006 f $<$6 GHz, SPS-020f $<$20 GHz) synthesizers are shown. The phase noise data was obtained from the manufacturer's datasheets.

The mixer required for the up-conversion is found inside a commercial I/Q mixer from Marki-Microwave (MMIQ-0520L). The I port input is used for the f_m signal input, and the Q port is terminated with a 50Ω load. The resulting DSB signal is amplified and combined with a portion of the original f_0 signal, as shown in Figure 1. The coupling element is a -3dB directional coupler, also known as a 2-way power divider from AAMCS (AAMCS-PWD-2W-5G-18G-10W-Sf). This setup permits a particularly strong f_0 presence in the three-tone input to the multiplier. A Spacek hextupler (AW-6XW) is used to bring the DSB signal into the W-band. The nonlinear nature of the $\times 6$ frequency multiplier creates a frequency comb with a central frequency $f_\mathrm{c} = 6f_0$ and inter-modulation products separated by f_m [25,30].

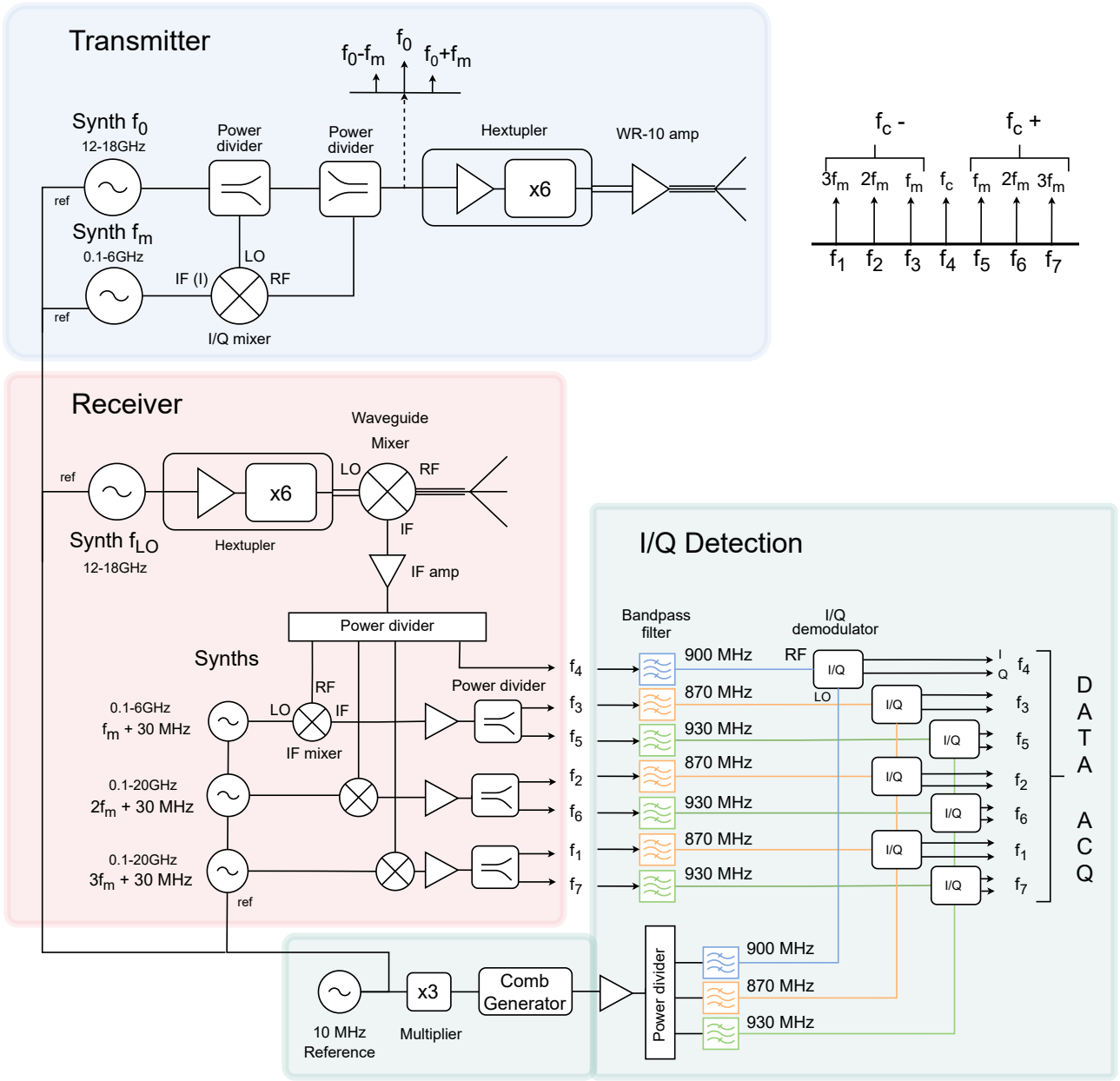

FIG. 1. Schematic diagram of the W-band frequency-comb DBS diagnostic. Refer to the text for further details on each sub-component as well as part numbers.

The output power of the hextupler is then strengthened by a WR-10 waveguide amplifier (SAGE Millimeter SBP-7531142515-1010-E1) prior to being sent to the tokamak. The amplifier is run at an input current exceeding the nominal value by 20%. This was done to ensure maximum gain and slightly saturate the amplifier, the latter leading to a small improvement in the output power flatness of the comb frequency components.

Both synthesizers feature fully programmable output frequency via Ethernet and USB. The high-frequency synthesizer controls the central frequency $f_c = 6f_0$ while the low-frequency unit controls the inter-frequency comb separation f_m. Moreover, both synthesizers feature output power control. The distribution of power to central and sideband signals in the three-tone signal is thus flexible. This flexibility is important because it provides the means to control the frequency-comb output power flatness. The non-linear nature of the hextupler leads to the frequency comb output power flatness being particularly sensitive to the DSB signal power balance. Optimal power settings for a relatively flat frequency comb output vary with specific values of both central and modulation frequencies. Section III shows that varying the output power of high and low-frequency synthesizers allowed for a $<$10 dB frequency comb power flatness for central frequencies anywhere inside the W-band and inter-frequency separations between $0.1-6$ GHz.

The receiver section is highlighted in red in Figure 1. It consists of a high-frequency synthesizer (NI-QuickSyn-FSW0020) used to drive an active W-band hextupler from SAGE (SFA-753114616-10SF-S1). The hextupler output is fed into the local-oscillator (LO) port of a W-band balanced mixer, also from SAGE (SFB-10-N1). This mixer down-converts the frequency-comb RF spectrum into IF frequencies between 0 and 35 GHz. The LO frequency is tuned above the central frequency f_c such that it down-converts f_c to an intermediate-frequency (IF) of 900 MHz (f_4 in Figure 1). The mixer's IF output is immediately followed by a low-noise (2 dB) high-gain (28 dB) amplifier (KLNA-00180M27A) and a 4-way power divider (Keylink KDIV001180M04A). The amplifier limits the IF frequency spectrum to less than 18 GHz. One of the splitter branches is sent immediately to the I/Q detection section without further treatment (f_4 in figure 1). Inside the I/Q detection section, a 900 MHz filter selects the central frequency for detection. In contrast, in order to measure frequencies surrounding f_c in the light of the tunable f_m separation, the receiver features an additional down-conversion stage. It consists of three tunable synthesizers and three down-conversion mixers.

The synthesizers are one low frequency ($<$6 GHz) SPS-06 and two high-frequency ($<$20 GHz) SPS-20 units from Spectran (see phase noise performance in Fig. 2). These are tuned to $f_m + \Delta f, 2f_m + \Delta f$, and $3f_m + \Delta f$, where Δf =30 MHz. Each respective f_m harmonic selects frequencies separated by an integer from the central frequency; for instance, $f_6 = f_c + 2f_m$ is selected by the second synthesizer with frequency $2f_m$+30 MHz. The Δf =30 MHz offset allows the separation of signals above and below f_c into 930 MHz and 870 MHz, respectively. The mixers are manufactured by Marki Microwave (T3-06/12/18). The mixer outputs are then amplified (25 dB gain, 2 dB NF from Keylink Microwave KLNA00106/112/118 0M27A) prior to being sent into the I/Q demodulation stage.

The I/Q detection section, shown in green in Figure 1, proceeds with IF filtering and I/Q detection of the scattered power in each frequency-comb signal. Firstly, the incoming signals are filtered by steep cavity band-pass filters (BPF) from Reactel Inc. (6C9) with a -1 dB rejection at $\pm$10 MHz, -30 dB at $\pm$15 MHz, and -60 dB at $\pm$30 MHz offset from the center frequency. The central frequency f_c signal, which comes directly from the first down-conversion, is filtered at 900 MHz. Three pairs of 870 and 930 MHz filters are used to select 3 pairs of frequencies above and below f_c, respectively. These have been color coded for clarity in Figure 1. The filtered signals are then coupled into the RF port of I/Q quadrature demodulators from Pulsar Microwave (ID-12-412). These feature an amplitude and phase balance of 0.8 dB and 6.0° max. These I/Q mixers extract the amplitude and phase of the backscattered signal by further mixing (down-converting) the filtered signals with a reference local-oscillator (LO). The LO signal for each I/Q mixer is generated as follows. Firstly, a 10 MHz ultra low noise crystal oscillator (Wenzel Associates Inc. 501-27521) is fed into an active low-noise odd order - $\times$3 - frequency multiplier (Wenzel LNOM-10-3-13-13-BT-BT). The resulting 30 MHz output drives a passive, step recovery diode based comb generator (TekBox - TBCG2). The latter creates a frequency comb with 30 MHz spacing between 1 MHz and 2.5 GHz, which includes the filter central frequencies required by the LO of I/Q mixers above. The output of the comb generator is amplified, split into three, filtered, and routed to the specific I/Q mixer as shown in the bottom right corner of Figure 1. The 10 MHz oscillator signal is also sent via a 8-way power divider (not shown in Figure 1 for clarity - MiniCircuits ZFSC-8-1) to each synthesizer to act as the reference oscillator in each unit. This ensures that all oscillators produce accurate frequencies and that the phase difference between all channels corresponds to the backscattered signal and not due to internal oscillator drifts in separate synthesizers. Each subsystem explained above was mounted in a separate 19-inch 3HE chassis with integrated active cooling via 8 cm diameter fans (EBM Pabst 8312 H). The real (I) and complex (Q) portions of the signal are then routed to SIO2 digitizers[32] which sample the analog output with a 16-bit resolution at 20 MSa/s. The digitized signals are sent to an acquisition computer via optical-fiber for storage in ASDEX-Upgrade's shot-file data storage system.

A. Potential interference

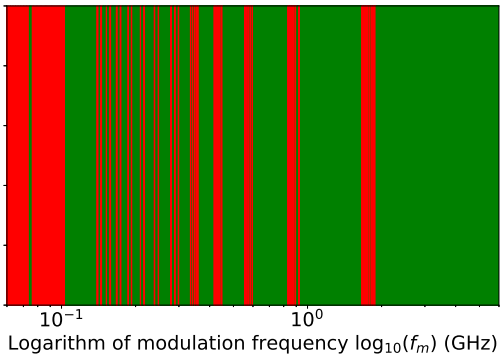

FIG. 3. Potential interference inside modulation frequency space. Red regions ilustrate potential interference while green represents modulation spaces free of interference. Note the logarithmic units in the x-axis.

The second mixer down-conversion process in the receiver stage, the large number of frequencies in the comb output, and the finite ±15 MHz (−30 dB) bandwidth of the filters in the I/Q stage may lead to unintentional interference. This is caused by image frequencies ($f_{IF} = f_{RF} \pm f_{LO}$[31][p. 638]) in the second-stage frequency down-conversion process and because the mixing process includes second and third harmonic LO frequencies created within the nonlinear mixing process. Although the latter are weaker, they can also lead to spurious signals. Figure 3 shows the results of a numerical scan of modulation frequencies where image frequencies at first, second, and third harmonics of each of the three second-stage IF mixer LOs are monitored for ambiguous frequency terms that intersect the frequency space of 870 and 930±15 MHz(−30 dB) filters. The central frequency (f4 in Fig. 1) using the 900 MHz BPF does not suffer from this potential interference because there is no second-stage down-conversion. As long as modulations under 30 MHz are not attempted, the 900 MHz filter does not suffer from potential interference.

Figure 3 shows that modulation frequencies under 105 MHz can lead to interference. It shows also that many potentially problematic modulation frequency regions exist under 2 GHz. No interference is found above 2 GHz. Using an arbitrary 6 MHz-step discretization inside the available 6 GHz modulation frequency space, potential interference was found in only 11% of the available frequency space. Thus, it does not prove a significant limitation in the operation of the diagnostic. Yet these potentially problematic modulation frequencies must be avoided during experiments. All modulation frequencies have been checked for the absence of interference prior to use in experiments.

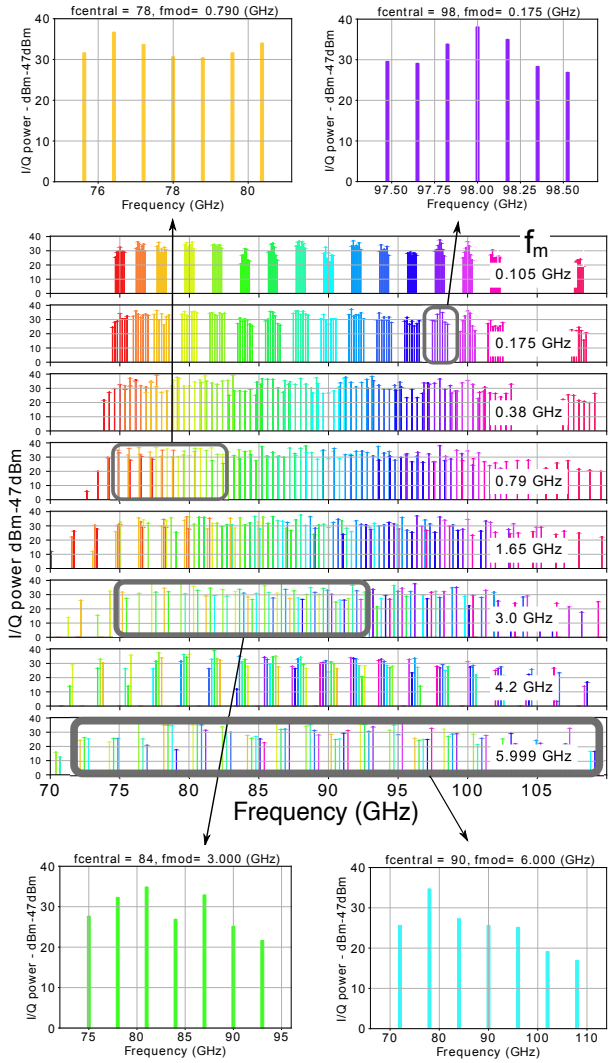

FIG. 4. Power-flatness tuning results demonstrating the ability of the diagnostic to produce 17 different central frequencies and 8 different modulation frequencies. Power measurements are taken at the I/Q mixer output with a test 500kHz frequency obtained via LO detuning. Power values are relative to −47 dBm which corresponds to a 1 mV noise floor, likely limited by the oscilloscope's ADC resolution.

III. POWER TUNING AND CALIBRATION

The performance of the diagnostic was tested in the laboratory prior to installation in AUG. In order to ensure a relatively flat frequency comb power output, the power of transmitter synthesizers f_0 and f_m was optimized for a range of output central frequency f_c and inter-frequency separations f_m.

In order to test the performance of the entire diagnostic including the entire receiver and I/Q detection hardware, the transmitter was connected directly to the receiver via a −40 dB waveguide attenuator and all 7 I/Q pair signals were monitored in the output of the I/Q detection section via a 14-channel oscilloscope. In order to mimic a Doppler shift from a plasma Doppler back-scattered signal and measure a

signal at the outputs of the I/Q detection module, the first-stage downconversion LO (f_{LO} in Fig. 1) was tuned 500 KHz off the regular LO frequency. Namely, if the central output frequency target was 60GHz, normally, the transmitter f_0 frequency would be 10 GHz and f_{LO} =10.15 GHz so that the central frequency's (f_c in Fig. 1) intermediate frequency sits exactly at 900 MHz. In order to create a test DBS signal in the laboratory, the f_{LO} was detuned by $500/6$ Khz to 10.149 916 666 GHz so that the resulting IF signal was 900.5 MHz. This 500 KHz signal off the central IF frequency carries through the system, goes through all BPFs ($\pm$30 MHz bandwidth) and is detected in the I/Q demodulators as a 500 KHz sinusoidal signal because the multiplier and comb generator in the I/Q detection module still create a constant 0.9 GHz LO reference regardless of the synthesizer's settings. The root-mean-square (rms) amplitude of the 500 kHz was measured at the output of each of the 7 I/Q demodulators, which provided a measurement of the amount of power present at each frequency term f_1 throguh f_7 in Fig. 1. Note that the amount of LO detuning is arbitrary (as long as it remains inside the BPF bandwith) and values of 20, 100, and 500 kHz were tested to give identical rms values in the output of all channels.

This setup allowed to perform a 'power-tunning' of the diagnostic where the output power of synthesizers f_0 and $f_{\rm m}$ in the transmitter module was varied until the output powers of the 7 I/Q mixers were found within a factor $\times 3$ of each other. This $\times 3$ voltage factor corresponds to a 10 dB power variation between frequency comb outputs. This power-tuning process was performed for central frequencies between 75$-$110 GHz with a 2 GHz spacing and for 7 different modulation frequencies between 0.1 and 6 GHz. Figure 4 shows the results of this power-tuning procedure. It shows that for low modulation frequencies $f_{\rm m}$ <1 GHz, all 7 channels can be made to lie within 10 dB of each other. Achieving 10 dB flatness becomes more difficult as the modulation frequency is increased. For instance, for $f_{\rm m}$ =1.65 GHz only 65% of central frequencies feature all 7 channels inside 10 dB, while 100% can match 6 out of 7 channels within 10 dB. At higher modulation frequencies such as $f_{\rm m}$ =5.99 GHz, many central frequency choices lead to the $3f_{\rm m}$ harmonics laying outside the W-band where power levels naturally decrease. Thus, the full 7-channel operation is only possible for central frequencies 92$-$94 GHz where 6 out of 7 frequencies lie within 10dB of each other.

Wang et al.[26] demonstrated a method to optimize the output flatness of the output comb spectrum by varying the relative phase between the IF input signals to the double-side-band modulator (see section II) whose output is then sent to the multiplier. A sufficiently broad-band phase-shifter could, unfortunately, not be procured as of the writing of this article. However, this method could be applied to this diagnostic in the future to improve the flatness of the output power spectrum.

All channels were tested to feature a linear response to input power from $-$10 dBm to $-$60 dBm: 50 dB, limited by the availability of variable waveguide attenuators. Theoretically, the dynamic range is expected at 96 dB. Power saturation was found to occur at 400 mV peak-to-peak voltage at the I/Q mixer output. The standard-deviation of each channel's voltage was recorded to provide a one-point power calibration value which permits to transform I/Q voltage values during experiments into equivalent scattered power levels. This calibration only takes into account power variations inherent to the diagnostic modules in Fig. 1 and does not include any frequency-dependant power variations caused by the transmission lines, mitter bends, vaccum window, and steerable antenna system[33]. A thorough in-vessel power calibration is left for future work.

IV. RESULTS

The diagnostic has been installed in AUG's sector 11 steerable antenna system[33] since December 2021. This antenna system is fully bistatic. The transmission lines consist of 8 m of oversized smooth-bore waveguides (3.8 cm diameter), 3 mitter bends, and a tilted quartz vacuum window to minimize reflections. The launcher antenna consists of two optimized smooth-bore antennas followed by two flat mirrors and one steerable ellipsoidal mirror facing the plasma. It has been designed to provide (in W-band) an E-field beam radius between $w_r = 2-3$ cm, a $\Delta k_\perp$ resolution of $\sim 2\,\mathrm{cm}^{-1}$, and a $k_\parallel/k_\perp$ fraction lower than 2% inside the outer mid-radius ($\rho = r/a \sim 0.6-1.0$) of typical AUG plasmas[33]. Both X and O-mode operation are possible. Thanks to the steerable mirror, operation as a perpendicular-incidence fluctuation reflectometer[34] is also possible.

Figure 5 shows the time traces, 7-channel diagnostic auto-power spectral density (APSD)[35], and inferred $v_\perp$ radial profiles during both 'low' (L) and 'high' (H) confinement regime[36] phases of shot 39987. The diagnostic was configured to output a central frequency of 83GHz with a modulation of 1.65GHz held constant during the shot. The poloidal angle of the launcher antenna was held constant at 18 deg pointing down from the horizontal. This led to scattering wavenumbers inside $k_\perp = 3.2-4.7\,\mathrm{cm}^{-1}$ during both L and H-mode phases. The discharge featured a core average density between 4.0×10^{19} and 7.2×10^{19} m^{-3}, deuterium gas fueling, a toroidal plasma current of $I_P = 0.8$MA (positive defined as counter-clockwise looking from the top), a toroidal magnetic field of -2.5 T, and external auxiliary heating power in the form of both electron cyclotron resonance heating (ECRH) (1.4 MW at 140GHz,second-harmonic X-mode) and neutral beam injection (NBI) (2.5 MW) as shown in fig. 5(a).

Figure 5(b) and fig. 5(c) permit to contrast the instantaneous APSD spectra during the L and H mode phases of discharge 33987. Beam-tracing simulations using the TORBEAM code[9] allowed for the computation of the scattering turning-point (sampling location) and wavenumber $k_\perp$. Only the path of the central beam is modeled; therefore, a ray-tracing calculation could have also been performed. The density profile used as input to TORBEAM was obtained from Thomson Scattering (TS)[37] measurements constrained by a 5 channel deuterium cyanide (DCN) laser interferometer. One core and two edge channels of the interferometer are plotted in Fig. 5(a). The standard CLISTE magnetic reconstruction

was also used as input to TORBEAM.

The L-mode spectra in fig. 5(b) show a very good signal-to-noise ratio (SNR) around ~ 30 dB. The different channels feature different Doppler shifts, which move towards zero Doppler shift with decreasing probing frequency and scattering location approaching the plasma separatrix ($\rho_{Pol} = 1$). The spectral width of the Doppler shift peak changes with scattering location: frequencies scattered closer to the separatrix $\rho_{Pol} = 0.979$ feature a Doppler shift peak with a $\sim$1 MHz full-width at half-max (FWHM) compared with ~ 0.5 MHz at $\rho_{Pol} = 0.79$. The peak power of the Doppler shifted spectra is also seen to vary with scattering location. The innermost scattering location features the lowest peak power, while the measured back-scattered power is largest at $\rho_{Pol} = 0.953$ and decreases slightly again in the outermost channels. While the power calibration has a sensitiviy of a few milli-Volts and hence sub-dB accuracy, there may be important frequency-dependant power variations in the quasi-optical launcher system that have not been taken into account. Therefore, the back-scattered power signals here are only indicative, and a full in-vessel calibration is required before these can be considered physically-meaningful differences in the measured back-scattered power. Nonetheless, changes to the spectral width and peak power of the Doppler shifted backscattered power hint interesting changes in turbulence properties over radius inside the L-mode phase. Full-wave synthetic diagnostics[38] applied to gyrokinetic simulations of this discharge can be used to quantitatively interpret the changes in density fluctuation properties with radius that lead to the observations presented here; however, these are beyond the scope of this paper.

The H-mode spectra in fig. 5(c) features important differences compared to fig. 5(b). Firstly, the spectra shows two main peaks. The first, centred around zero frequency, is likely due to power reflected in perpendicular incidence from the plasma cutoff. This peak is often neglected in the analysis of DBS signals. The second peak observed is likely due to backscattered power redshifted by $2-4$ MHz. The backscattered peak power decreases significantly to ~ 10 dB down from ~ 30 dB. This decrease in fluctuation level is consistent with the widely accepted model for the H-mode transport barrier being caused by a strong ExB velocity shear[39] that leads to edge turbulence suppression. Furthermore, due to the creation of a steep edge density 'pedestal'[40] in H-mode, all frequencies scatter much closer to the separatrix and in much closer proximity to one another than in fig. 5(b). The Doppler shifts observed in fig. 5(c) are also found in closer proximity between the different frequencies. Moreover, the backscattered power measured is lower in channels closer to the separatrix and appears to increase as the frequencies climb into the pedestal. It should be noted that the H-mode spectra in fig. 5(c) were taken inside a time period in-between edge-localized modes(ELMs)[41] to avoid perturbing the APSD. Experimental evidence of various pedestal-localized modes have been reported across many tokamaks[42], which may be behind the lack of symmetry in the Doppler shits in fig. 5(c) for channels 5-7. Careful interpretation of these observations is left for future work.

Figure 5(d) shows the $v_\perp$ radial profiles inferred from Doppler shifts in figures fig. 5(b) and fig. 5(c) and TORBEAM simulations. Wavenumber uncertainties of $\Delta k = 2\,\mathrm{cm}^{-1}$ are found to dominate the $v_\perp$ error bars. The L-mode and H-mode $v_\perp$ rotation profiles are highly distinct because the Doppler shifts measured changed significantly. Wavenumbers are found inside $k_\perp 3.2-4.7\,\mathrm{cm}^{-1}$ during both L and H-mode phases.

Figure 6 shows the spectrogram from all 7-channels accross the L-H mode transition of 39987. The transition occurs at about $t \simeq 2.07$ s shortly after NBI heating is introduced at $t = 1.99$ s, and it is marked by a vertical cyan line in fig. 6. Interferometer signals measuring line-integrated edge (DCN 4, 5) and core (DCN 0) average densities show a marked simultaneous increase in plasma density, which results from the particle transport barrier created in the edge region of H-mode plasmas[36]. Doppler spectra in fig. 6 show marked changes in the backscattered power and Doppler shift around the L-H mode transition. The momentum input from NBI is immediately observed in all channels after 2.0 s through changes in the Doppler shift. The L-H mode transition results in rapid changes in the spectra of frequencies under 83.0 GHz where it seems to transition between spectra resembling fig. 5(b) to fig. 5(c) almost instantly. After the L-H transition, the scattered powers drop significantly and Doppler shifts transition rapidly from $f_D \sim 0-1$ MHz to about $f_D = -3--4$ MHz. Frequencies above 83 GHz do not immediately change which indicates that the L-H transition leads to fast changes in edge conditions but not deeper inside the plasma.

Figure 6 demonstrates that time-resolved *simultaneous* multi-point DBS measurements can reveal important radial dynamics of both density fluctuation properties as well as plasma rotation which are not available in single-frequency instruments. The observation that the H-mode transition begins in the edge and builds-up towards the core is consistent with fast density measurements of L-H transitions[43] which show that the edge transport barrier leads to a steady build-up of the pedestal that is not immediate and grows from the edge into the core. The diagnostic presented here can be easily adapted to either focus in a particular section or sample a wider range of the pedestal. Currently, the comb frequencies are only adjusted remotely in-between discharges. However, changes to the frequency configuration can be performed inside a discharge with external triggering of pre-programmed synthesizer frequency trajectories available in all synthesizer units. The demonstration of this functionality is left for future work.

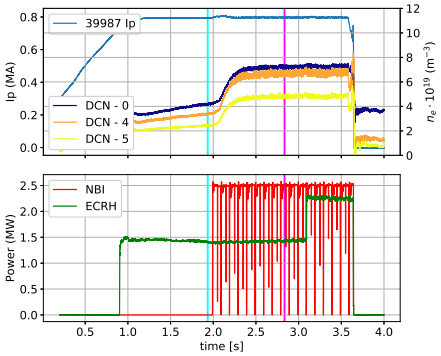

(a)

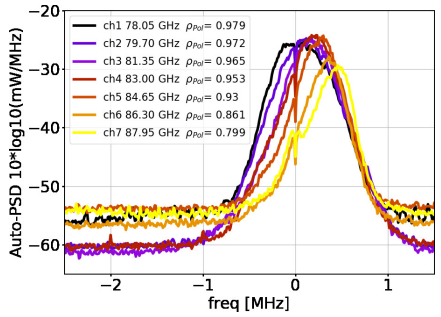

(b)

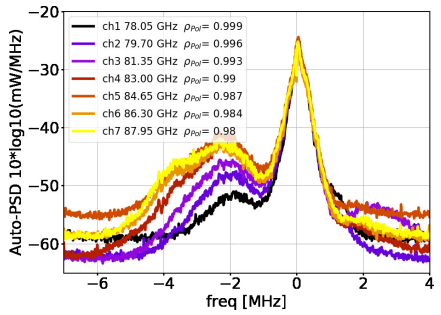

(c)

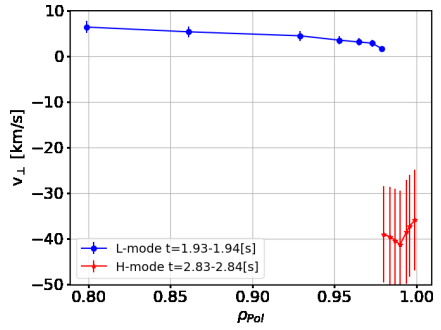

(d)

FIG. 5. 5(a) Top: time traces of plasma current (I_p) and line average density along the plasma core (DCN 0) and plasma edge (DCN 4, 5). Bottom: time traces of external heating power sources. In red and in green neutral beam injection (NBI) and electron cyclotron resonance heating (ECRH), respectively. 5(b) Comb backscattered signal 2-sided APSD spectra during L-mode 1.93-1.94s and 5(c) H-mode 2.83-2.84s. 5(d) Radial profiles of $v_\perp$ during both L (b) and H-mode (c) phases of the discharge. Scattering wavenumbers range inside $k_\perp = 3.4 - 4.5\text{cm}^{-1}$ in both L and H-mode phases.

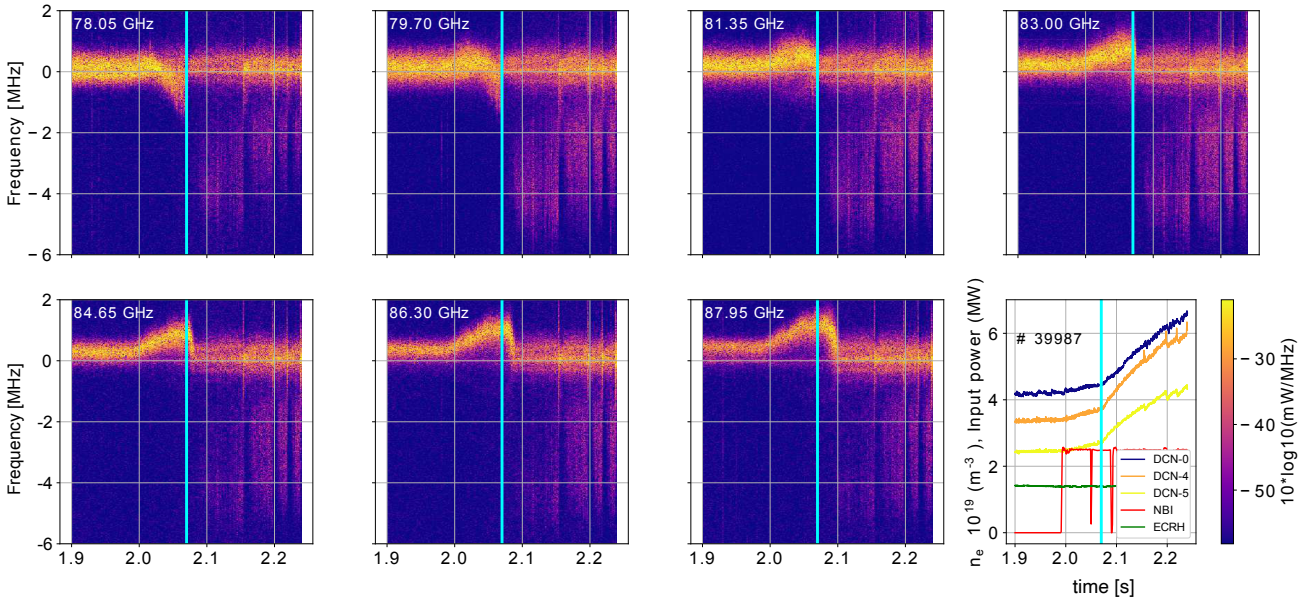

FIG. 6. 7ch spectrogram across the L-H mode transition in shot 39987.

V. SUMMARY

In summary, a fully tunable, multi-frequency, 'comb' W-band Doppler backscattering system has been developed, tested, and deployed in the AUG tokamak. It measures the backscattered power from 7 separate frequencies simultaneously using I/Q demodulation and regular 10 MHz bandwidth digitizers. These 7 frequencies can sit anywhere inside the W-band, and the inter-frequency spacing can be varied between $0.1-6$ GHz. In order to change the location and/or inter-frequency spacing, no hardware changes are required, only the remote programming of 6 low-frequency synthesizers via ethernet. Laboratory tests have verified that the output power flatness of the frequency comb can be made to stay inside <10 dB by carefully controlling the double-side band input signal to a x6 varactor multiplier. First data shows signal-to-noise ratios in excess of 30 dB during L-mode plasmas at wavenumbers inside $k_\perp = 3.5-4.5$ cm^{-1}. The time evolution of backscattered signals from 7 simultaneous frequencies across the L-H transition of discharge 39987 demonstrates the unique potential of multi-point measurements to access the physics both density fluctuations and plasma rotation during fast plasma events.

ACKNOWLEDGMENTS

This work has been carried out within the framework of the EUROfusion Consortium, funded by the European Union via the Euratom Research and Training Programme (Grant Agreement No 101052200 — EUROfusion). Views and opinions expressed are however those of the author(s) only and do not necessarily reflect those of the European Union or the European Commission. Neither the European Union nor the European Commission can be held responsible for them.

[1] A. Herrmann and O. Gruber, Fusion Science and Technology **44**, 569 (2003).
[2] E. Holzhauer, M. Hirsch, T. Grossmann, B. Brañas, and F. Serra, Plasma Physics and Controlled Fusion **40**, 1869 (1998).
[3] E. Z. Gusakov and A. V. Surkov, Plasma Physics and Controlled Fusion **46**, 1143 (2004).
[4] E. Blanco and T. Estrada, Plasma Physics and Controlled Fusion **50**, 095011 (2008).
[5] T. Happel, T. Görler, P. Hennequin, C. Lechte, M. Bernert, G. D. Conway, S. J. Freethy, C. Honoré, J. R. Pinzón, U. Stroth, and The ASDEX Upgrade Team, Plasma Physics and Controlled Fusion **59**, 054009 (2017).
[6] J. R. Pinzón, T. Happel, E. Blanco, G. D. Conway, T. Estrada, and U. Stroth, Plasma Physics and Controlled Fusion **59**, 035005 (2017).
[7] J. C. Hillesheim, W. A. Peebles, T. L. Rhodes, L. Schmitz, T. A. Carter, P.-A. Gourdain, and G. Wang, Review of Scientific Instruments **80**, 083507 (2009).
[8] P. Hennequin, R. Sabot, C. Honoré, G. T. Hoang, X. Garbet, A. Truc, C. Fenzi, and A. Quéméneur, Plasma Physics and Controlled Fusion **46**, B121 (2004).
[9] E. Poli, A. Bock, M. Lochbrunner, O. Maj, M. Reich, A. Snicker, A. Stegmeir, F. Volpe, N. Bertelli, R. Bilato, G. Conway, D. Farina, F. Felici, L. Figini, R. Fischer, C. Galperti, T. Happel, Y. Lin-Liu, N. Marushchenko, U. Mszanowski, F. Poli, J. Stober, E. Westerhof, R. Zille, A. Peeters, and G. Pereverzev, Computer Physics Communications **225**, 36 (2018).
[10] M. Hirsch, E. Holzhauer, J. Baldzuhn, and B. Kurzan, Review of Scientific Instruments **72**, 324 (2001).
[11] J. Schirmer, G. D. Conway, E. Holzhauer, W. Suttrop, H. Zohm, and t. A. U. Team, Plasma Physics and Controlled Fusion **49**, 1019 (2007).
[12] G. D. Conway, B. Scott, J. Schirmer, M. Reich, A. Kendl, and t. A. U. Team, Plasma Physics and Controlled Fusion **47**, 1165 (2005).
[13] J. Pinzón, T. Happel, P. Hennequin, C. Angioni, T. Estrada, A. Lebschy, U. Stroth, and the ASDEX Upgrade Team, Nuclear Fusion **59**, 074002 (2019).
[14] J. R. Pinzón, T. Estrada, T. Happel, P. Hennequin, E. Blanco, and U. Stroth, Plasma Physics and Controlled Fusion **61**, 105009 (2019).
[15] L. Cupido, J. Sánchez, and T. Estrada, Review of Scientific Instruments **75**, 3865 (2004).
[16] F. Wagner, Plasma Physics and Controlled Fusion **49**, B1 (2007).
[17] A. W. Leonard, Physics of Plasmas **21**, 090501 (2014).
[18] T. Estrada, C. Hidalgo, T. Happel, and P. H. Diamond, Physical Review Letters **107**, 245004 (2011).
[19] W. A. Peebles, T. L. Rhodes, J. C. Hillesheim, L. Zeng, and C. Wannberg, Review of Scientific Instruments **81**, 10D902 (2010).
[20] R. Soga, T. Tokuzawa, K. Watanabe, K. Tanaka, I. Yamada, S. Inagaki, and N. Kasuya, Journal of Instrumentation **11**, C02009 (2016).
[21] T. Tokuzawa, S. Inagaki, A. Ejiri, R. Soga, I. Yamada, S. Kubo, M. Yoshinuma, K. Ida, C. Suzuki, K. Tanaka, T. Akiyama, N. Kasuya, K. Itoh, K. Watanabe, H. Yamada, K. Kawahata, and LHD Experiment Group, Plasma and Fusion Research **9**, 1402149 (2014).
[22] J. Q. Hu, C. Zhou, A. D. Liu, M. Y. Wang, E. J. Doyle, W. A. Peebles, G. Wang, X. H. Zhang, J. Zhang, X. Feng, J. X. Ji, H. Li, T. Lan, J. L. Xie, W. X. Ding, W. D. Liu, and C. X. Yu, Review of Scientific Instruments **88**, 073504 (2017).
[23] Z. Shi, W. Zhong, M. Jiang, Z. Yang, B. Zhang, P. Shi, W. Chen, J. Wen, C. Chen, B. Fu, Z. Liu, X. Ding, Q. Yang, and X. Duan, Review of Scientific Instruments **87**, 113501 (2016).
[24] Z. Shi, W. Zhong, Z. Yang, A. Liang, J. Wen, M. Jiang, P. Shi, B. Fu, C. Chen, Z. Liu, X. Ding, and Q. Yang, Review of Scientific Instruments **89**, 10H104 (2018).
[25] P. Molina Cabrera, S. Coda, L. Porte, N. Offeddu, P. Lavanchy, M. Silva, M. Toussaint, and TCV Team, Review of Scientific Instruments **89**, 083503 (2018).
[26] M. Y. Wang, C. Zhou, A. D. Liu, J. Zhang, Z. Y. Liu, X. Feng, J. X. Ji, H. Li, T. Lan, J. L. Xie, S. Q. Liu, W. X. Ding, W. Z. Mao, G. Zhuang, and W. D. Liu, Review of Scientific Instruments **89**, 093501 (2018).
[27] X. Feng, A. D. Liu, C. Zhou, M. Y. Wang, J. Zhang, Z. Y. Liu, Y. Liu, T. F. Zhou, S. B. Zhang, D. F. Kong, L. Q. Hu, J. X. Ji, H. R. Fan, H. Li, T. Lan, J. L. Xie, W. Z. Mao, Z. X. Liu, W. X. Ding, G. Zhuang, and W. D. Liu, Review of Scientific Instruments **90**, 024704 (2019).
[28] X. H. Ren, Z. J. Yang, Z. B. Shi, Z. C. Yang, X. Q. Zha, Y. Gao, and Z. C. Zhang, Review of Scientific Instruments **92**, 033545 (2021).
[29] T. Tokuzawa, S. Inagaki, M. Inomoto, A. Ejiri, T. Nasu, T. I. Tsujimura, and K. Ida, Applied Sciences **12**, 4744 (2022).
[30] T. Happel, W. Kasparek, P. Hennequin, K. Höfler, C. Honoré, and the ASDEX Upgrade Team, Plasma Science and Technology **22**, 064002 (2020).
[31] D. M. Pozar, *Microwave Engineering*, 4th ed. (Wiley, Hoboken, NJ, 2012).
[32] K. Behler, H. Eixenberger, and A. Lohs, in *12th IAEA TM on Control, Data Acquisition, and Remote Participation for Fusion Research* (Daejeon, Korea, 2019).
[33] T. Happel, G. D. Conway, W. Kasparek, and B. Plaum, in *Proc. 10th Intl. Reflectometry Wksh. - IRW10* (Padova, 2011).
[34] E. Mazzucato, Review of Scientific Instruments **69**, 2201 (1998).
[35] J. Bendat and A. Piersol, *Random Data: Analysis and Measurement Procedures*, 1st ed. (John Wiley and Sons, Inc., 1971).
[36] F. Wagner, G. Becker, K. Behringer, D. Campbell, A. Eberhagen, W. Engelhardt, G. Fussmann, O. Gehre, J. Gernhardt, G. v. Gierke, G. Haas, M. Huang, F. Karger, M. Keilhacker, O. Klüber, M. Kornherr, K. Lackner, G. Lisitano, G. G. Lister, H. M. Mayer, D. Meisel, E. R. Müller, H. Murmann, H. Niedermeyer, W. Poschenrieder, H. Rapp, H. Röhr, F. Schneider, G. Siller, E. Speth, A. Stäbler, K. H. Steuer, G. Venus, O. Vollmer, and Z. Yü, Physical Review Letters **49**, 1408 (1982).
[37] B. Kurzan and H. D. Murmann, Review of Scientific Instruments **82**, 103501 (2011).
[38] C. Lechte, G. D. Conway, T. Görler, T. Happel, and the ASDEX Upgrade Team, Plasma Science and Technology **22**, 064006 (2020).
[39] K. H. Burrell, Physics of Plasmas **4**, 1499 (1997).

[40]R. J. Groebner and T. H. Osborne, Physics of Plasmas **5**, 1800 (1998).
[41]H. Zohm, Plasma Physics and Controlled Fusion **38**, 105 (1996).
[42]F. Laggner, A. Diallo, M. Cavedon, and E. Kolemen, Nuclear Materials and Energy **19**, 479 (2019).
[43]P. A. Molina Cabrera, B. Labit, S. Coda, and L. Porte, Plasma Physics and Controlled Fusion **63**, 085019 (2021).